Acta Mech 232, 1479–1496 (2021)
https://doi.org/10.1007/s00707-020-02913-2

ORIGINAL PAPER

Zhijie Yu · Zhongya Lin · Yueguang Wei

Investigation on cross-scale indentation scaling relationships of elastic–plastic solids

Received: 13 July 2020 / Revised: 23 September 2020 / Accepted: 6 December 2020 / Published online: 16 February 2021

Abstract Indentation scaling relationships provide normalized guidance for measuring and predicting mechanical properties in indentation experiments. At the nano-scale, the material size-effect is significant, while conventional scaling relationships fail to depict this phenomenon in nanoindentation precisely. In the present research, cross-scale indentation scaling relationships are investigated using a strain gradient theory. The nanoindentation response is found to be sensitive to different material parameters, including the material intrinsic length, yield stress, and work-hardening exponent across size-scales. If the strain gradient effect is ignored, the nanoindentation scaling relationships approach the macroscopic conventional ones. The cross-scale indentation scaling relationships obtained in the form of dimensionless functions in this work provide quantitative references to instrumented indentation tests on multiple size-scales, coinciding well with experimental results. The understanding of nanoindentation hardness is enhanced by the present work.

1 Introduction

The indentation test is an extensively used material testing technique to determine the properties of macroscopic bulk materials and novel nano-materials [1–4]. The indentation test quickly obtains material properties by instrumented experiments within a local area of the material. This advantage is especially remarkable when performing tests on a small size-scale, where other methods, e.g., tension, bending, and torsion, are difficult to implement technically. Hence the indentation test methods have attracted extensive attention in the past decades [5–7].

Much emphasis has been put on research works of the methods, techniques, and especially the precision and normalization of the instrumented indentation tests. For macroscopic indentation tests, with the benefit of the self-similarity of the conical indenter, Cheng et al. suggested a series of indentation scaling relationships considering many aspects of the elastic–plastic material properties [8–12]. These results are widely used to explain indentation results and understand the physical meaning of the indentation hardness. Also, with the help of the indentation scaling relationships, determining material properties from experiments and validating numerical indentation results become more accessible and reliable. The scaling approach also guides indentation tests of various materials and multiple research fields, exhibiting greater expansibility than individual instrumented experiments [13, 14]. Kang and Yan performed a study on the indentation scaling relationships in shape memory alloys [15]. Rodriguez et al. researched the amorphous materials by the scaling approach from experiments of multiple samples [16]. Bazzaz et al. implemented the scaling analysis and numerical simulation to test the alloy thin film [17]. The scaling relationships help to analyze and discuss the indentation results more intuitively.

Z. Yu · Z. Lin · Y. Wei (✉)
Department of Mechanics and Engineering Science, College of Engineering, BIC-ESAT, Peking University, Beijing 100871, China
e-mail: weiyg@pku.edu.cn

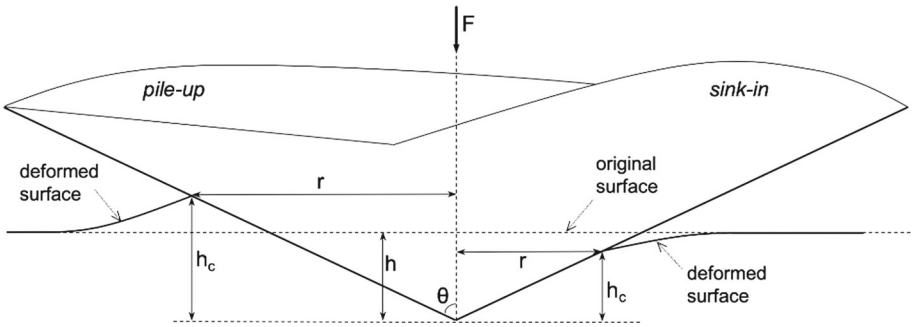

Fig. 1 Illustration of the conical indentation, (left) pile-up $h_c > h$, (right) sink-in $h_c < h$

Moreover, many specific works have also been performed based on the convenience and intuitiveness of the indentation scaling relationships [18, 19]. Li et al. developed an analytical software for a new portable instrumented indentation device using multiple approaches including the scaling approach [20]. Recently, Yu and Wei studied the scaling relationships considering the influence of the inclusion near the indenter tip in macroscopic bulk materials [21]. Besides the straightforward application of the scaling relationships, the spirit of this indentation scaling approach is also adopted and integrated with novel research interest [22]. Zhang et al. suggested an indentation method to test a hyper-elastic soft biomaterial with the scaling analysis [23]. Lee et al. combined the scaling approach with the artificial neural network to investigate the properties of materials from indentation tests [24].

In recent years, mechanical behavior measurements of micro- or nano-structured materials as well as conventional materials at the nano-scale also attract much research interest. Many investigations showed different properties of materials among size-scales [25, 26]. This size-effect also emerges in most testing methods. Micro- and nano-scale testing techniques, represented by atomic force microscope (AFM) and nanoindentation, have therefore been further used to measure the size-effects [5, 27]. Many size-dependent nanoindentation results have been presented and discussed [7, 28, 29]. Corresponding theories and methods emerged rapidly in order to characterize the nanoindentation test results [30, 31]. Fisher has reviewed the nanoindentation test on film coating materials [32]. Recently, Lin et al. suggested a measurement method for polymers considering the indenter tip adhesion effects of AFM [33]. Long et al. used reverse analysis and numerical simulation to study the material properties in nanoindentation [34]. Novel phenomena have also been exhibited in the indentation tests at small size-scales [35–38]. Yang et al. have reviewed the recent progress and challenges in determining the size-effect in nanoindentation [39]. Nevertheless, many macroscopic theories and methods, including the scaling method of the indentation scaling relationships, face considerable challenges in handling novel materials at the nano-scale and advanced nano-testing techniques [40]. The indentation scaling relationships of an elastic–plastic solid considering the material size-effect remain blank.

In the present work, a strain gradient-based model [41] is used to depict the size-effect during the nanoindentation process, which well characterizes the cross-scale behavior of elastic–plastic materials [42–45]. With the dimensional analysis and the corresponding finite element analysis [46, 47], the cross-scale indentation scaling relationships can be presented in the form of dimensionless functions, extending the reference value of the macroscopic indentation scaling relationships to multiple size-scales. Comparisons of the cross-scale indentation scaling relationships with several nanoindentation experimental results are also presented, which exhibits a good coincidence and validates the present work.

2 Model description

2.1 Indentation model

The conical indentation is illustrated in Fig. 1. When a load F is applied, the indenter penetrates the materials with vertical displacement h. The contact depth h_c represents the actual interaction depth between the indenter and the indented material, and correspondingly the radius of the projected contact area is r. $h_c > h$ represents the pile-up phenomenon, as illustrated in the left part of Fig. 1, and $h_c < h$ represents sink-in, shown in the right part of the Figure.

The half-angle of the conical indenter is taken to be 68°, which is commonly adopted in similar studies of the indentation scaling relationships [48–50], and this is a close estimate of either Vickers or triangular pyramidal indenters. Assuming the indenter tip is ideally sharp, this problem is perfectly self-similar in geometry. The conical indenter is assumed to be rigid. The interface between the indenter and the material is assumed to be frictionless unless otherwise stated [51].

2.2 Constitutive model

Metals and metal-based composite materials have a wide range of mechanical and non-mechanical applications at the micro- and nano-scale [52, 53]. A straightforward constitutive model for metals is the elastic–plastic model combined with certain work-hardening. However, since no parameter on the length-dimension exists, the conventional elastic–plastic theories cannot describe the size-effect of materials. To extend this widely used method to multiple size-scales, a size-relevant strain gradient plasticity model (CMSG) suggested by Huang et al. [41] is adopted in this work.

The detailed derivation of the CMSG model is appended in Appendix A, and a brief illustration is introduced below. Equation (1) shows the stress–strain relation between flow stress σ_{flow}, plastic strain ε^p, and plastic strain gradient η^p, where E denotes the elastic modulus, Y the initial yield stress, n the power-law work-hardening exponent, and l the material intrinsic length,

$$\sigma_{\text{flow}} = Y \cdot \sqrt{\left(1 + \frac{E\varepsilon^p}{Y}\right)^{2n} + l\eta^p}. \tag{1}$$

Together with Poisson's ratio ν, the material can be determined by the parameters mentioned above. In the present work, the range of material parameters is selected similarly with Cheng et al. [8], namely, Y/E has a value between 0.001 and 0.1, n between 0 and 0.5, and ν between 0.2 and 0.4. The range of the material intrinsic length is related to the maximum indentation depth, which will be discussed in part 2.3.

2.3 Dimensional analysis

With the application of the Π theorem [47, 54], the primary dependent variables, the load F and the contact depth h_c, can be expressed as functions of other independent variables by

$$F = f_\alpha(E, Y, \nu, n, l, \theta, h), \tag{2}$$

$$h_c = f_\beta(E, Y, \nu, n, l, \theta, h). \tag{3}$$

A constant maximum indentation depth $h_{\max}$ is set for all indentation tests. Among the above variables and constants, at least two independent dimensions are necessary to describe all other ones as

$$\begin{aligned} &[F] = [E]^1 \cdot [h]^2, \\ &[Y] = [E]^1 \cdot [h]^0, \\ &[h_c] = [h_{\max}] = [l] = [E]^0 \cdot [h]^1, \\ &[n] = [\theta] = [\nu] = [E]^0 \cdot [h]^0. \end{aligned} \tag{4}$$

Hence, the load F and the contact depth h_c can be expressed by

$$F = Eh^2 \cdot \Pi_1\left(\frac{Y}{E}, \frac{l}{h_{\max}}, \nu, n, \theta\right), \tag{5}$$

$$h_c = h \cdot \Pi_2\left(\frac{Y}{E}, \frac{l}{h_{\max}}, \nu, n, \theta\right), \tag{6}$$

and all variables in Π_1 and Π_2 are dimensionless.

The indentation hardness H is another most concerned material parameter in indentation tests, which is defined by Eq. (7), and correspondingly written in its dimensionless form by Eq. (8),

$$H = \frac{F}{A} = \frac{F}{\pi r^2} = \frac{F}{\pi h_c^2 \tan^2\theta}, \tag{7}$$

$$
\begin{aligned}
H &= \frac{F}{\pi h_c^2 \tan^2\theta} = \frac{Y}{Y} \cdot \frac{1}{\pi \tan^2\theta} \cdot \frac{Eh^2 \cdot \Pi_1}{(h \cdot \Pi_2)^2} \\
&= Y \cdot \left(\frac{E}{Y} \cdot \frac{1}{\pi \tan^2\theta} \cdot \frac{\Pi_1}{\Pi_2^2} \right) \\
&\triangleq Y \cdot \Pi_3 \left(\frac{Y}{E}, \frac{l}{h_{\max}}, \nu, n, \theta \right).
\end{aligned} \tag{8}
$$

In some circumstances, the hardness can also be nondimensionalized by the elastic modulus as

$$
\begin{aligned}
H &= \frac{F}{\pi h_c^2 \tan^2\theta} = \frac{E}{\pi \tan^2\theta} \cdot \frac{h^2 \cdot \Pi_1}{(h \cdot \Pi_2)^2} \\
&\triangleq E \cdot \Pi_4 \left(\frac{Y}{E}, \frac{l}{h_{\max}}, \nu, n, \theta \right).
\end{aligned} \tag{9}
$$

The range of material constants Y/E, ν, n, and a fixed half-angle θ were given previously. And the last material constant is the material intrinsic length l, which is then given a value in the range of $0 \le l/h_{\max} \le 100$. The material intrinsic length is the parameter characterizing the size-effect of materials. The material intrinsic length of most metals is around microns; therefore, the range given above covers most nano-, micro-, and even macroscopic indentation tests. A larger dimensionless material intrinsic length represents that the extent of the material size-effect is stronger, or correspondingly, the indentation test is implemented at a smaller size-scale. Particularly, $l/h_{\max} = 0$ represents cases that ignore the material size-effect, which is consistent with Cheng et al.'s previous works [8, 12].

2.4 Finite element model

To evaluate the dimensionless functions and illustrate the scaling relationships given above, finite element analysis is implemented on ABAQUS 6.14 [46], with the usage of the user material subroutine (UMAT) for the constitutive model mentioned in 2.2 and Appendix A. The finite element model consists of 17,351 axisymmetric 4-node continuum elements. The meshes not only reach the mesh convergence but also have a proper distribution to capture the deformation and the strain gradient near the indenter. All cases share the same mesh division when the material parameters vary, keeping the numerical error to a minimum. The indentation area is relatively small enough to minimize the influence of the model boundary.

3 Results and discussion

Based on the dimensionless functions derived previously, the result of the indentation scaling relationships can be collected into figures of the dimensionless functions. The indentation scaling relationships and influences of material properties are summarized qualitatively and quantitatively. An experimental application is also implemented on some metal materials.

3.1 Intuitive influence of the material size-effect

Figure 2 shows the relationship between the dimensionless functions Π_1, Π_2, Π_3 and the dimensionless indentation depth, with a fixed Poisson's ratio and dimensionless yield stress. Larger $l/h_{\max}$ represents intenser material size-effect. The black line is plotted based on the size-independent model of Cheng et al. [8]. The size-effect is significant in materials of $l/h_{\max} \ge 1$, and the dimensionless functions are depth-sensitive during indentation. It also shows that when the material intrinsic length is more considerable, the contact depth is smaller while the indentation load is larger. Hence, the indentation hardness ascends distinctly when the dimensionless material intrinsic length increases, up to ten times that of the macroscopic result. Besides, the $l/h_{\max} \ne 0$ cases gradually degenerate to the $l/h_{\max} = 0$ case with increasing indentation depth.

The influence of the material size-effect on the dimensionless functions is monotonic, as shown in Fig. 2. Therefore, each curve can be integrated into one single data point by its mean value throughout the entire indentation process. Using this scheme, cases with a minimum value $l/h_{\max} = 0$ and a maximum value $l/h_{\max} = 100$ are plotted in Fig. 3 with different power-law work-hardening exponents n and Poisson's ratios ν. Results in Fig. 3a coincide well with that of the same result of Cheng et al. [8]. In Fig. 3a and b, it is shown that

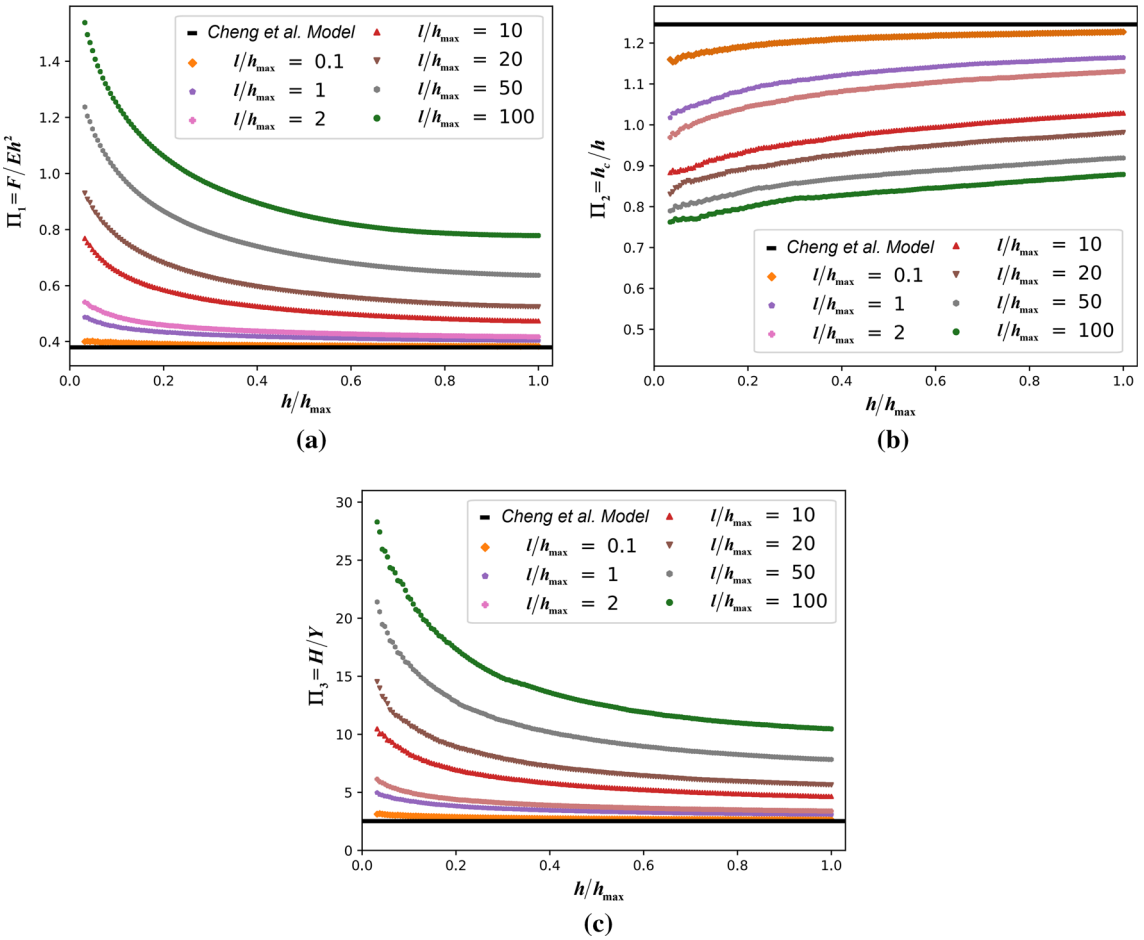

Fig. 2 Dimensionless functions, **a** dimensionless load Π_1, **b** dimensionless contact depth Π_2, **c** dimensionless hardness Π_3, against the indentation depth at different dimensionless material intrinsic lengths, with $\nu = 0.3$, $n = 0$, $Y/E = 0.005$. Different symbols represent the extent of the material size-effect ($l/h_{\max}$). Larger $l/h_{\max}$ represents the more evident size-effect, where the material is more indentation depth-dependent

the material size-effect comprehensively raises the indentation hardness, especially one with smaller power-law work-hardening exponent n and lower dimensionless yield stress Y/E. In Fig. 3c and d, noting that the value of the Y-axis is different, it can also be found that materials of any Poisson's ratio ν all have higher indentation hardness when the material size-effect is considered. The influence of Poisson's ratio is found not as significant as other material parameters. Hence in the following discussion, ν is fixed at $\nu = 0.3$. Generally, whether the material size-effect is considered or not, the work-hardening exponent influences the hardness more significantly when the dimensionless yield stress is lower, while Poisson's ratio influences a bit only when Y/E is relatively large. And specifically, for materials of intense size-effect ($l/h_{\max} = 100$) and a relatively large dimensionless yield stress ($Y/E \geq 0.04$), the dimensionless indentation hardness shows no relevance with the work-hardening exponent. In such cases of intense size-effect, the indentation scaling relationships shifts a lot, and the macroscopic dominating material parameter n will not affect the nanoindentation hardness anymore.

3.2 Influence of the material intrinsic length

The monotonicity of the material size-effect is comparatively intuitive. Hence the quantitative analysis is needed to capture when and how its influence involves. Relationships between dimensionless functions Π_1, Π_2, Π_3, and the material intrinsic length with different work-hardening exponents are plotted in Fig. 4. All three dimensionless functions are found deviated from the Cheng et al. size-independent scaling relationships when

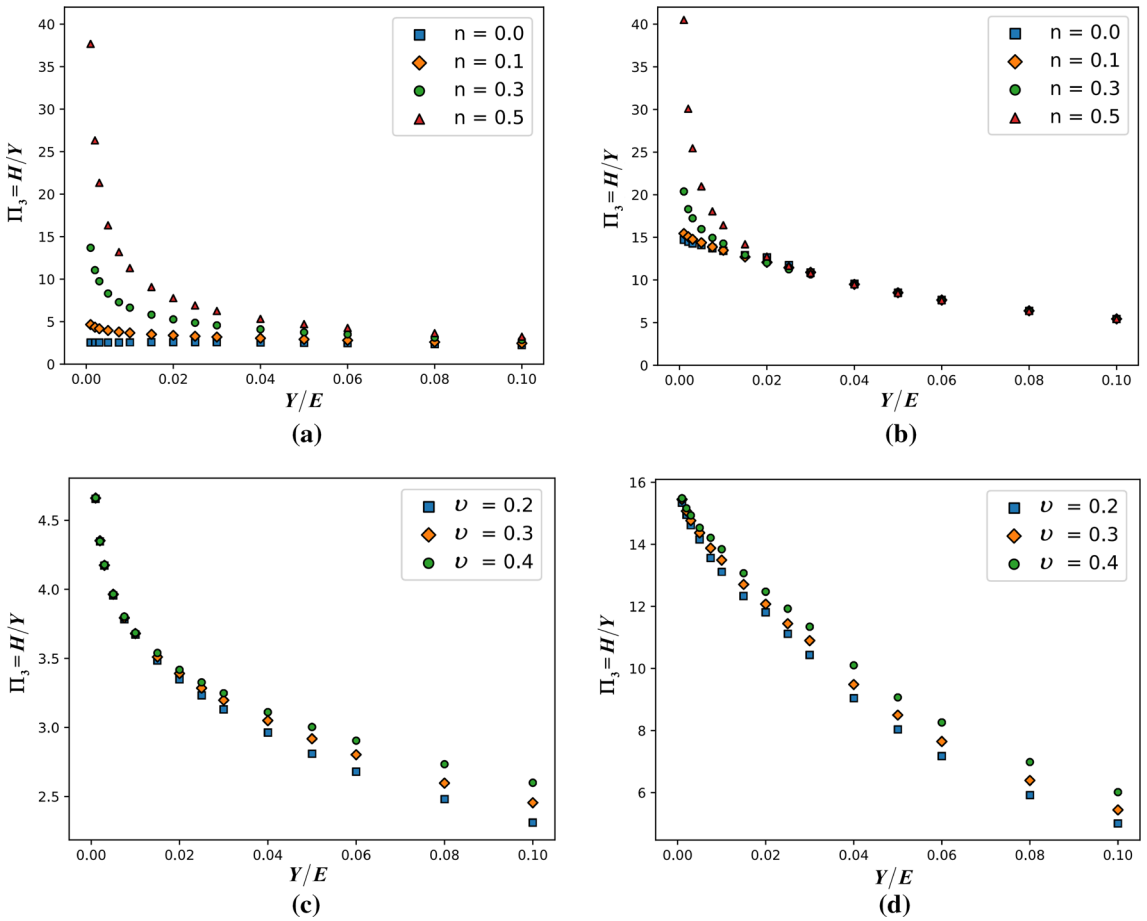

Fig. 3 Dimensionless hardness Π_3 of the size-independent model of Cheng et al. [8] (**a** & **c**), and with the consideration of the size-effect (**b** & **d**). The work-hardening exponent varies with fixed $\nu = 0.3$ (**a** & **b**), and Poisson's ratio varies with fixed $n = 0.1$ (**c** & **d**). Each symbol represents the mean value of the dimensionless hardness throughout each single indentation test (h from 0 to $h_{\max}$). The work-hardening induced material hardening is suppressed when the size-effect is considered (**a** & **b**). The influence of Poisson's ratio is not as distinguishable as the work-hardening exponent and the dimensionless yield stress (**c** & **d**). Note that the value of the Y-axis is different in (**c**) and (**d**)

the material size-effect becomes stronger. And this size-dependent deviation is larger in materials of less work-hardening effect. The material size-effect is found to start influencing the dimensionless functions at a relatively low value when the work-hardening effect is insignificant. Materials without work-hardening begin to respond when $l/h_{\max} \geq 10^{-1}$, while typical work-hardening materials respond earlier since $l/h_{\max} \geq 10^{1}$. Hence in the next Figure, the range of $l/h_{\max}$ is chosen to be $10^{-1} \leq l/h_{\max} \leq 10^{2}$. In addition, the size-effect suppresses the influence of different work-hardening exponents, especially in the dimensionless contact depth.

Figure 5 shows the relationships between the dimensionless indentation hardness and the size-effect ($l/h_{\max}$) of different materials. Larger work-hardening exponent and material intrinsic length both enlarge the indentation hardness. The hardening effect of the material work-hardening is evident only when the dimensionless yield stress is low, whereas the hardening from the size-effect is more uniform for all materials. For those materials without work-hardening, the difference of hardness is ignorable among various yield stresses when the size-effect is not considered. However, the intenser material size-effect generates a more significant difference of hardness among materials of different yield stresses after $l/h_{\max} \geq 1$.

3.3 Scaling relationships related to the dimensionless yield stress

Relationships between dimensionless functions and yield stress also need to be discussed in detail with different material size-effects considered. Figure 6 shows the dimensionless hardness at different work-hardening

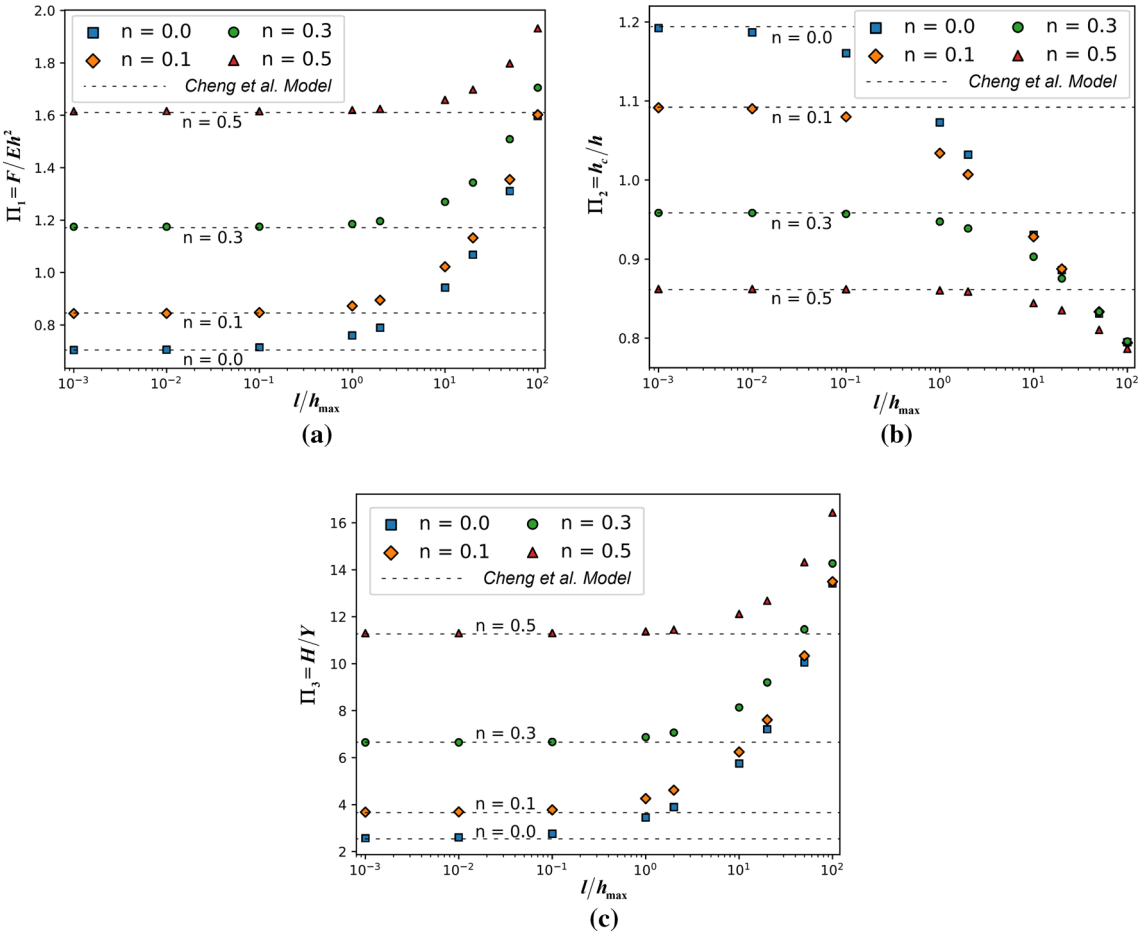

Fig. 4 Dimensionless functions **a** Π_1, **b** Π_2, **c** Π_3 against dimensionless material intrinsic length $l/h_{\max}$ with $\nu = 0.3$ and $Y/E = 0.01$. Results from the size-independent model of Cheng et al. [8] are given in the dashed lines. The scaling relationships gradually deviate with the increasing material size-effect. When $l/h_{\max}$ or n is larger, the dimensionless load and hardness are larger, while the contact depth is smaller

exponents and different material intrinsic lengths. The black line at the bottom is the result of the Cheng et al. size-independent model. It can be found that materials of lower yield stress are more sensitive to the work-hardening effect. The influence of the size-effect is more considerable in materials of lower dimensionless yield stress when the work-hardening exponent is small (Fig. 6a and b). When the work-hardening effect is intense (Fig. 6c and d), materials of medial dimensionless yield stress become most size-sensitive. Moreover, for materials without work-hardening, as shown in Fig. 6a, their dimensionless indentation hardness seems to have no relution with the yield stress when $l/h_{\max} = 0$, but linear relations appear when the size-effect is considered.

From Eq. (8), the dimensionless hardness is calculated from the dimensionless load and contact depth. Therefore, to find out the cause of the hardness response, the dimensionless load and contact depth are plotted, respectively, in Figs. 7 and 8. Four subfigures in Fig. 7 show little difference with each other. Compared with the indentation load, the dimensionless contact depth exhibits divergent patterns, as shown in Fig. 8. The work-hardening effect reduces the contact depth, while this phenomenon is magnified when the material size-effect is considered. To be specific, the dimensionless contact depth of materials of lower yield stress decreases more evidently when the work-hardening exponent is small ($n = 0, 0.1$), while less evidently when it is large ($n = 0.3, 0.5$). Materials of lower yield stress are generally more sensitive to the work-hardening effect and the size-effect. However, when the yield stress is small and the work-hardening exponent is large ($Y/E = 0.001, n = 0.5$), the material size-effect seems no longer affecting the indentation contact depth, as well as the indentation load. This answers the result in Fig. 6d that the indentation hardness of the material with $Y/E = 0.001, n = 0.5$ varies in a narrow range of $H/Y = 27(\pm 10\%)$ with different extent of the size-effect.

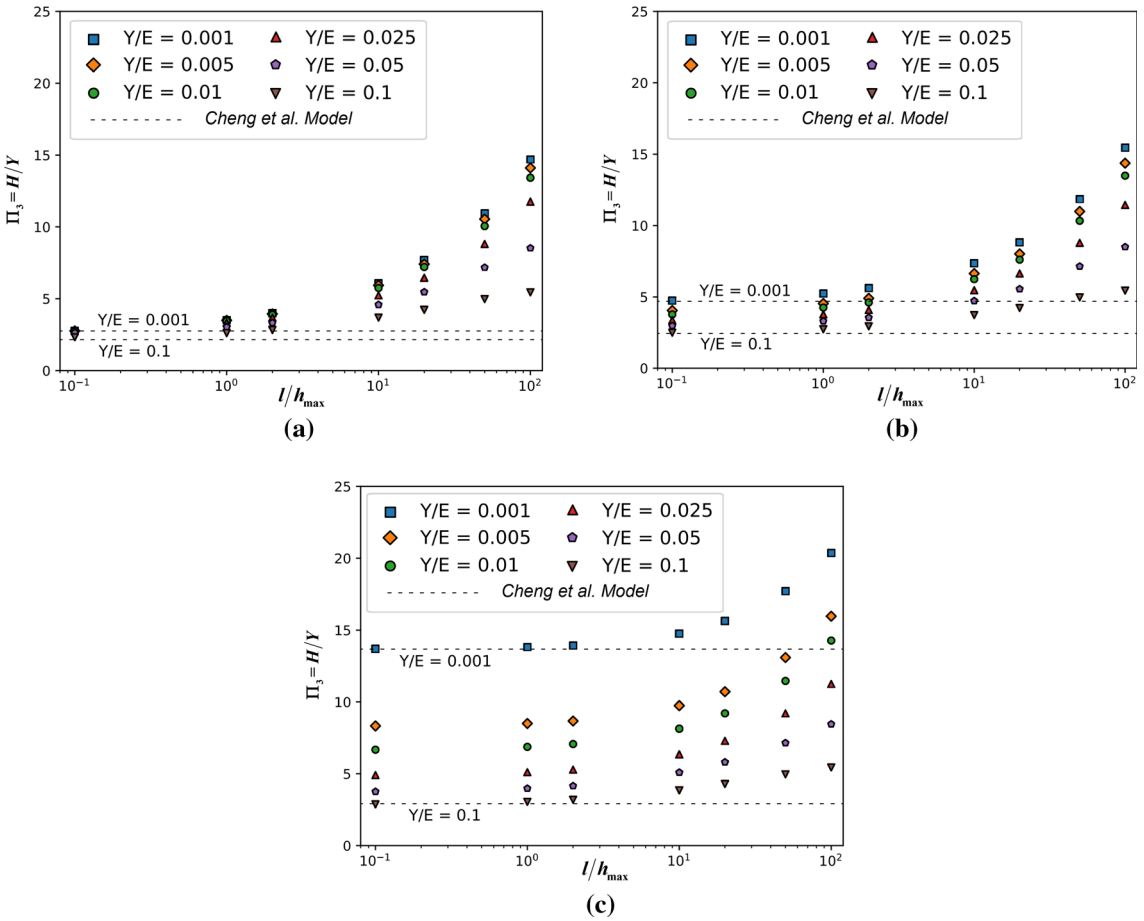

Fig. 5 Dimensionless hardness Π_3 against dimensionless material intrinsic length $l/h_{\max}$ with $\nu = 0.3$ and **a** $n = 0$, **b** $n = 0.1$, **c** $n = 0.3$. The size-independent model of Cheng et al. [8] is presented in dashed lines of $Y/E = 0.001, 0.1$ for compactness. Dimensionless hardness ascends rapidly with increasing dimensionless material intrinsic length

In contrast, for other materials, the influence of the material size-effect is usually enlarged to 100% or even more. From Figs. 7 and 8, it can be inferred that the nanoindentation hardness is even more influenced by the contact morphology rather than the indentation load.

Figure 9 exhibits the relationships of dimensionless hardness $\Pi_4 = H/E$ as in Eq. (9). The material size-effect comprehensively raises the dimensionless hardness, and also gradually minimizes the influence of the work-hardening effect. Moreover, whether considering the material size-effect or not, materials of higher dimensionless yield stress exhibit less relativity with the work-hardening exponent. When the size-effect is evident (Fig. 9c), the work-hardening effect does not influence the materials of a high dimensionless yield stress.

3.4 Effect of friction across size-scales

The influence of friction between the indenter and the material surface is briefly exhibited in Fig. 10. It can be found that the influence of friction is becoming smaller when the material size-effect becomes stronger. Difference between the frictionless case and the friction considered cases are about 20% when the size-effect is ignorable, while that is only at about 3 ~ 5% when the friction is considered together with the size-effect. The reason is that the friction affects indentation by resisting the tangential deformation at the contact surface; however, this deformation has been restricted by the hardening effect of the work-hardening as well as the material size-effect. It has been indicated that the friction needs to be concerned when a considerable pile-up phenomenon happens ($h_c/h > 1.12$), when $h_c/h \leq 1.12$, the frictionless assumption might be a reasonable approximation [51, 55].

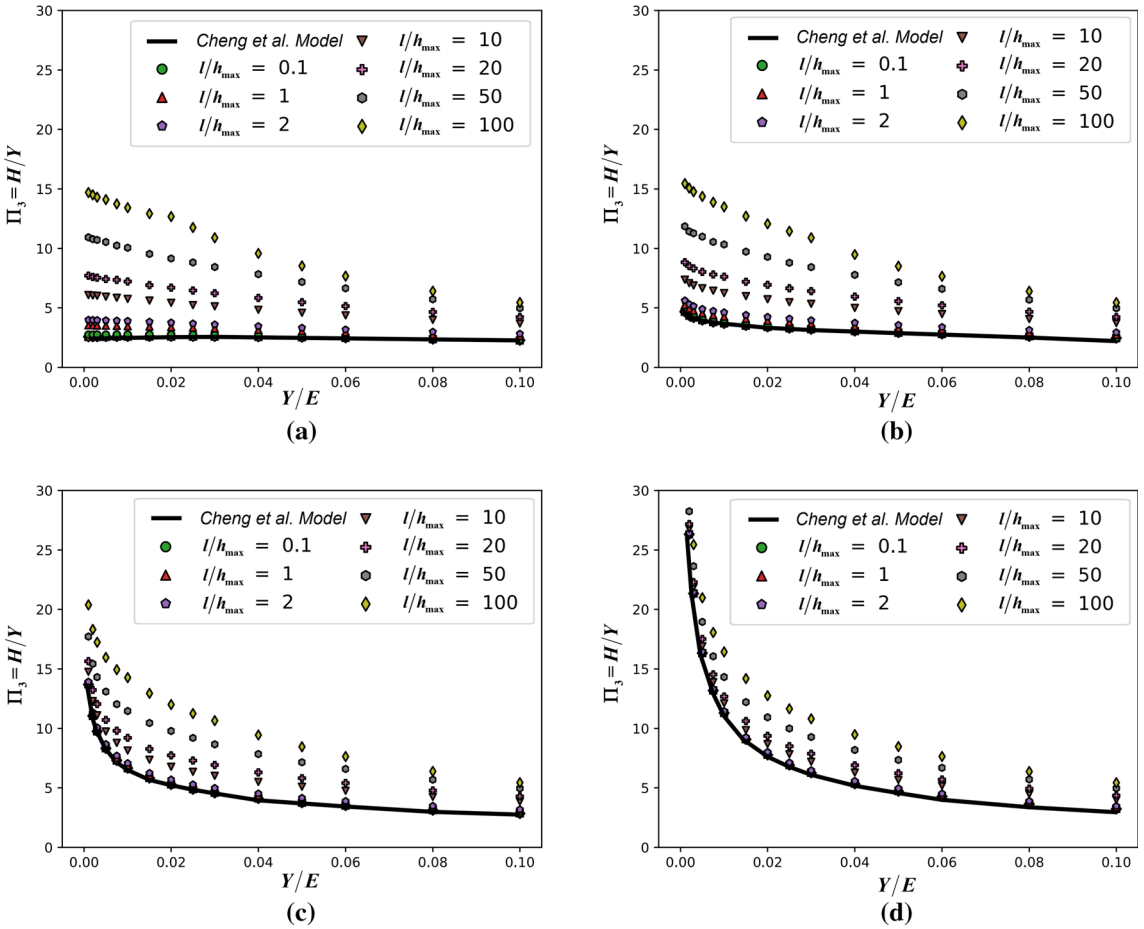

Fig. 6 Dimensionless hardness Π_3 against dimensionless yield stress Y/E for different $l/h_{\max}$ with $\nu = 0.3$, **a** $n = 0$, **b** $n = 0.1$, **c** $n = 0.3$, **d** $n = 0.5$. The baseline of the size-independent model [8] is plotted in black lines. The hardness, nondimensionalized by the initial stress Y, decreases when the dimensionless yield stress increases. This trend is more evident in materials of larger work-hardening exponent

3.5 Application on instrumented nanoindentation

One of the remarkable applications of the scaling relationships is to predict the instrumented indentation experiments. The results of most nanoindentation tests are intensely size-dependent at an indentation depth from tens of nanometers to several micrometers [28, 29, 56–63]. The nanoindentation hardness of these materials against the dimensionless indentation depth is shown in Fig. 11 together with the corresponding scaling relationships. The experimental results better coincide with the cross-scale scaling relationships throughout the entire indentation process compared with the conventional size-independent model. Experiments of Al by Wei et al. [56] and Cu by McElhaney et al. [61] have a different dimensionless material intrinsic length (calculated by Eq. (19) in "Appendix A") of 8 and 4, whose influence on the dimensionless hardness is more evident when the indentation depth is smaller. The hardness tested from instrumented indentation is a bit higher than the prediction of scaling relationships when the indentation depth is small, and a kind of lower when that is large, while the mean value coincides better with the indentation scaling relationships.

The mean value of the dimensionless hardness during the indentation of more experimental results is plotted in Fig. 12. The dimensionless yield stress of these metal materials is generally $0.001 \leq Y/E \leq 0.01$. The experimental results well match the prediction of the indentation scaling relationships across size-scales. The dimensionless material intrinsic length has a broad application range of the indentation depth from microns to tens of nanometers. With the integration of the indentation depth and the material intrinsic length, the prediction and validation of instrumented indentation at different size-scales can be much easier. By using the

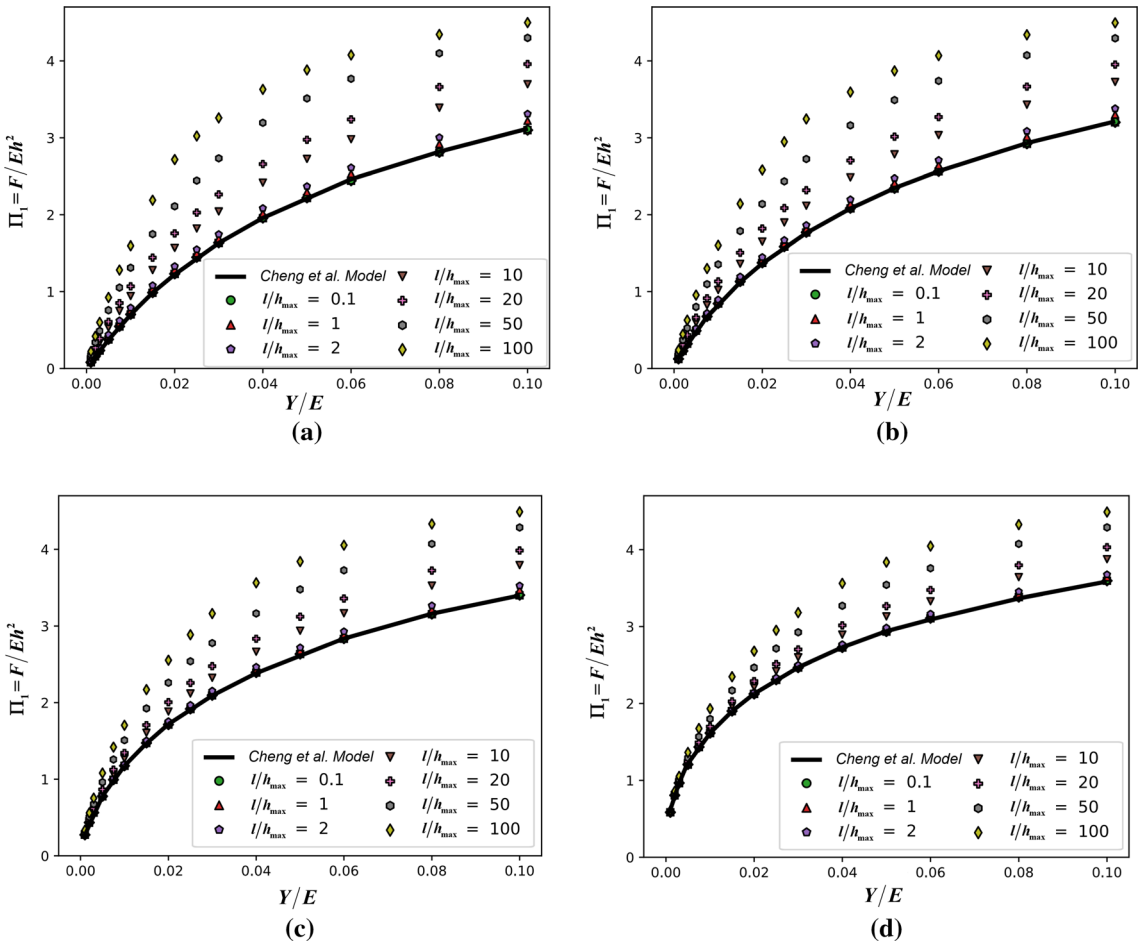

Fig. 7 Dimensionless load Π_1 against dimensionless yield stress Y/E of different $l/h_{\max}$ with $\nu = 0.3$ and **a** $n = 0$, **b** $n = 0.1$, **c** $n = 0.3$, **d** $n = 0.5$. The baseline of the size-independent model [8] is plotted in black lines. The dimensionless load is higher in materials of larger dimensionless yield stress and intrinsic length. This trend changes very little among materials of different work-hardening exponents

cross-scale indentation scaling relationships, the result of an arbitrary indentation depth can be used to estimate the corresponding result of any other indentation depth, significantly reducing the experiment workload.

4 Conclusions

In the present work, the cross-scale indentation scaling relationships are proposed with the application of a size-dependent constitutive model. This cross-scale result can be therefore applied to multiple size-scales, extending the usage of the macroscopic indentation scaling relationships. The relative comparison between the scaling relationships with and without the material size-effect is discussed in detail. The deviation caused by the material size-effect is quantitatively captured. The hardness and the associated load and contact depth are discussed separately. Many quantitative results can be extracted directly from the Figures of those dimensionless functions, guiding the indentation test at multiple size-scales.

The material size-effect affects the macroscopic scaling relationships by increasing the indentation load and reducing the contact area; hence, the nanoindentation hardness ascends significantly. As the indentation depth increases, the size-effect considered results approach the macroscopic ones. Specifically, when the material yield stress is relatively low, the power-law work-hardening exponent has considerable influence on the indentation hardness. For the size-effect involved materials of a high yield stress, the influence from the work-hardening is ignorable. Furthermore, the influence of the size-effect works differently in materials of different yield stress and work-hardening exponent. Materials of lower yield stress and lower work-hardening

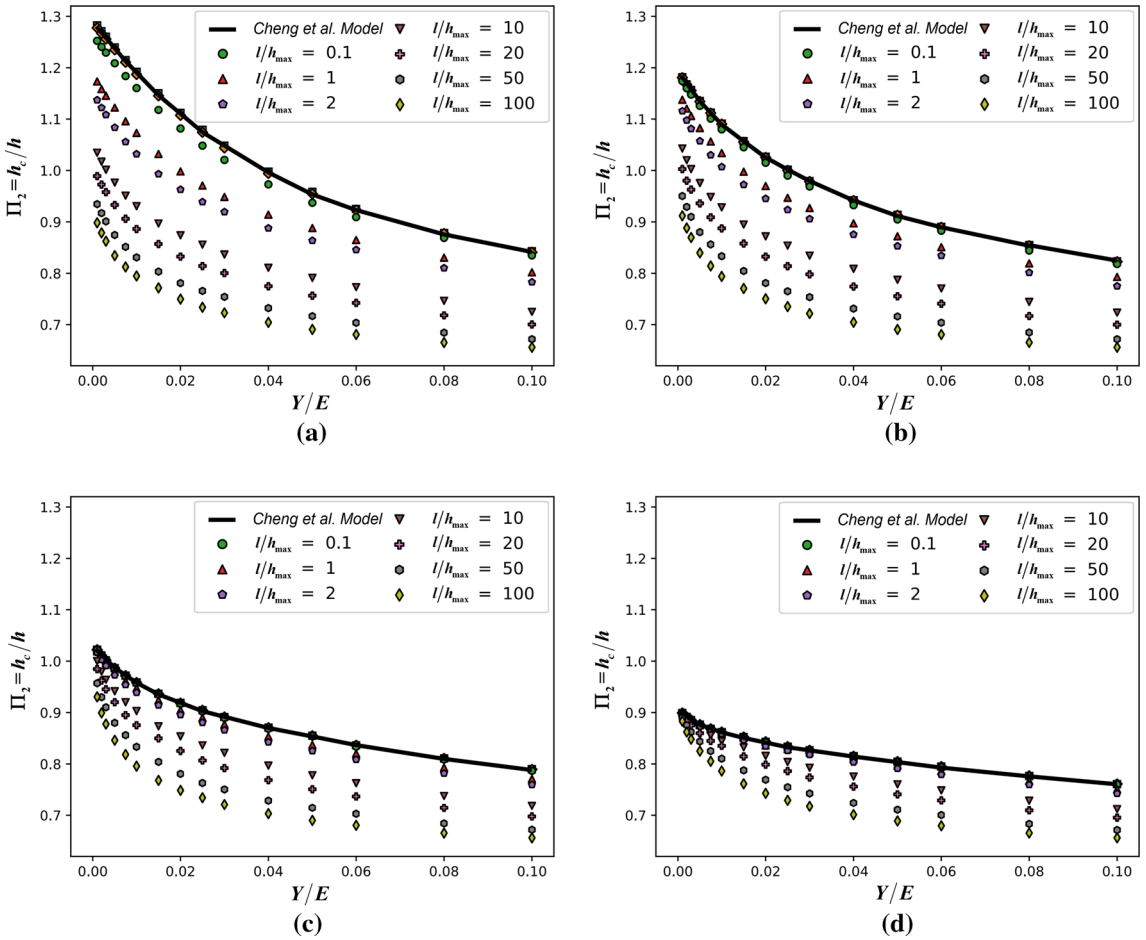

Fig. 8 Dimensionless contact depth Π_2 against dimensionless yield stress Y/E of different $l/h_{\max}$ with $\nu = 0.3$ and **a** $n = 0$, **b** $n = 0.1$, **c** $n = 0.3$, **d** $n = 0.5$. The baseline of the size-independent model [8] is plotted in black lines. The dimensionless contact depth is lower when the dimensionless intrinsic length or yield stress is larger. The influence of the intrinsic length is distinct in materials of any yield stress when the work-hardening exponent is low, while only evident in materials of low yield stress when the work-hardening effect is strong

exponent are more likely to be affected by the size-effect. In comparison, those with lower yield stress but higher work-hardening exponent are almost irrelevant for the size-effect. The material size-effect also weakens the role the work-hardening effect plays but enhances that of the yield stress. Therefore, materials of different properties and size-scales have different dominating parameters: the dimensionless yield stress dominates the indentation response when the work-hardening exponent is large; the dimensionless material intrinsic length dominates when the dimensionless yield stress or material intrinsic length itself is considerable; the work-hardening exponent dominates when the dimensionless yield stress or material intrinsic length is small. Capturing these dominating parameters helps to evaluate the indentation test with the least effort. The nondimensionalized material intrinsic length makes it possible to predict the result of any indentation depth from a test of arbitrary depth.

At the nano-scale, the significant increase in nanoindentation hardness is caused by the increase of the indentation load on the one hand and the rapid decrease of the contact area on the other hand. Meanwhile, the friction between the indenter and material surface is found to be less influential compared with the material size-effect. The decrease in the contact area also answers why the friction affects less when the size-effect is more remarkable.

A procedure for indentation tests at multiple size-scales is presented by the results of the dimensionless functions with the consideration of the material size-effect. Furthermore, the quantitative results can be used to instruct instrumented indentation tests across size-scales or alternatively estimate the material intrinsic length

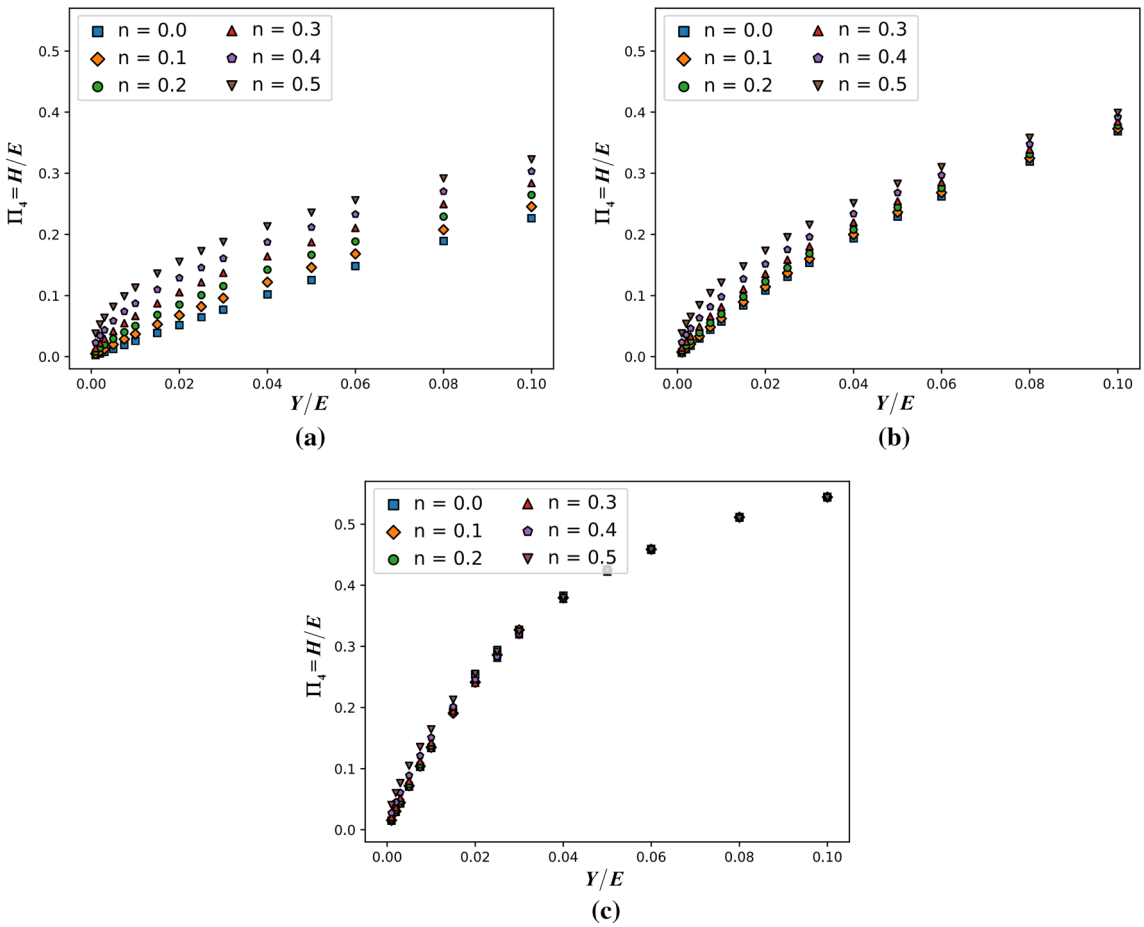

Fig. 9 Dimensionless hardness Π_4 against dimensionless yield stress Y/E of different n with $\nu = 0.3$ and **a** $l/h_{\max} = 0$ (Cheng et al. size-independent model [8]), **b** $l/h_{\max} = 10$, **c** $l/h_{\max} = 100$. The hardness, nondimensionalized by the elastic modulus, increases with the dimensionless yield stress. When $l/h_{\max}$ is larger, the dimensionless hardness is higher but less affected by the work-hardening effect

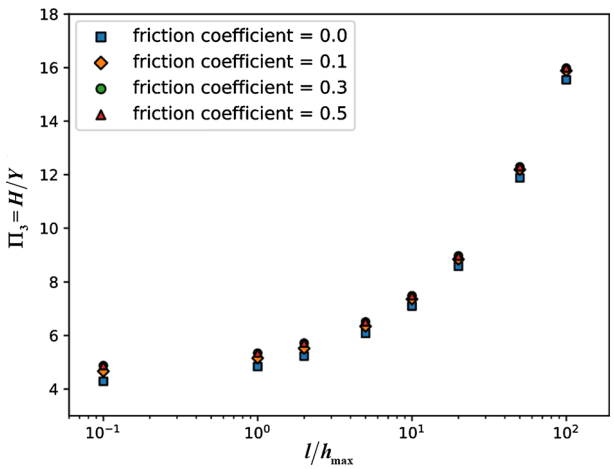

Fig. 10 Dimensionless hardness Π_3 against dimensionless material intrinsic length $l/h_{\max}$ with different friction coefficient between the indenter and material surface. Other material parameters are $Y/E = 0.003$, $\nu = 0.3$, and $n = 0.1$. The influence of friction is restricted by the material size-effect

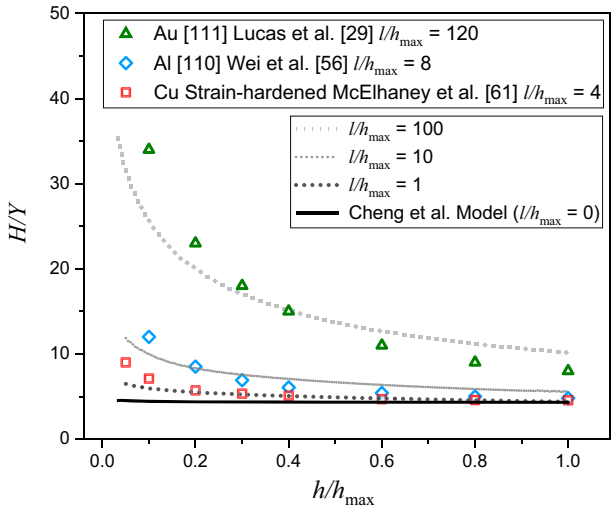

Fig. 11 Nanoindentation hardness Π_3 against the dimensionless indentation depth of some metal materials and corresponding scaling relationships. Lines are for the same material parameters as in Fig. 2c except for n=0.1 and $Y/E = 0.002$

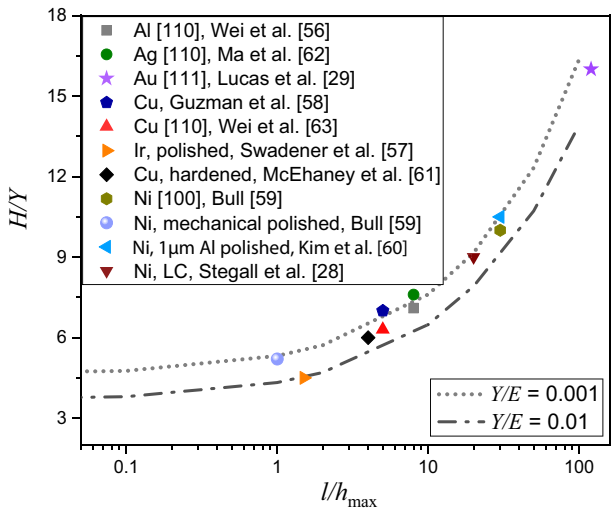

Fig. 12 Nanoindentation hardness Π_3 against the dimensionless material intrinsic length of some metal materials and corresponding scaling relationships. Lines are for the same material parameters as in Fig. 5 of n=0.1

experimentally. The qualitative deduction also helps to design and test novel materials in various size-scales and enhances the understanding of the indentation hardness across size-scales.

Acknowledgements This work is supported by the NSF of China through Grants Nos. 11890681, 12032001, 11672301 and 11521202.

Appendix A: Conventional theory of mechanism-based strain gradient

Multiple material models have been suggested by many researchers to overcome the limitation that the conventional theory failed to predict the size-effect of materials. A strain gradient term together with a length-dimension parameter were introduced into the continuum constitutive relation, which was suggested by many scholars [64, 65]. Wei and Hutchinson performed a strain gradient plasticity theory on the crack growth and fracture problem [66], and Nix and Gao applied it with the indentation of crystalline materials [42]. Gao et al. proposed a mechanism-based strain gradient plasticity (MSG) theory [67, 68] established from the Taylor dis-

location model [69, 70]. This mechanism-based theory gave a reasonable explanation of the length parameter introduced by the strain gradient. Based on the MSG theory, Huang et al. introduced a conventional theory of mechanism-based strain gradient plasticity (CMSG) [43, 44, 71, 72], which avoids the higher-order boundary conditions and hence is more feasible than earlier theories.

The taylor dislocation model gives the relation between dislocation density and the shear flow stress τ as

$$\tau = \alpha\mu b\sqrt{\rho} = \alpha\mu b\sqrt{\rho_S + \rho_G} \tag{10}$$

where b is the magnitude of the Burgers vector, and μ the shear modulus, α an empirical parameter taking a value in the range from 0.2 to 0.5 for most materials, and ρ the total dislocation density, composed by the statistically stored dislocation (SSD) density ρ_S and the geometrically necessary dislocation (GND) density ρ_G.

The flow stress σ_{flow} is related to the shear flow stress by

$$\sigma_{flow} = M\tau = M\alpha\mu b\sqrt{\rho_S + \rho_G} \tag{11}$$

with the Taylor factor $M = 3.06$ for most face-centered-cubic (fcc) metals. In the uniaxial test, ρ_S can be determined where ρ_G equals zero,

$$\rho_S = \left(\frac{\sigma_{flow}}{M\alpha\mu b}\right)^2, \tag{12}$$

and ρ_G is related to the effective plastic strain gradient η^p by

$$\rho_G = \bar{r}\frac{\eta^p}{b} \tag{13}$$

introduced by Nye with a factor of $\bar{r} = 1.90$ for fcc metals. Thus, in a microscopic view, the flow stress is

$$\sigma_{flow} = M\tau = M\alpha\mu b\sqrt{\rho_S + \bar{r}\frac{\eta^p}{b}}. \tag{14}$$

Meanwhile, in a macroscopic view, the flow stress is also

$$\sigma_{flow} = \sigma_Y f\left(\varepsilon^p\right) \tag{15}$$

where σ_Y is the initial yield stress, ε^p is the effective plastic strain, and the function f between them can be determined by the uniaxial tension test. One of the most used models is the power-law work-hardening model,

$$f\left(\varepsilon^p\right) = \left(1 + \frac{E\varepsilon^p}{\sigma_Y}\right)^n, \tag{16}$$

where E is the elastic modulus and n the work-hardening exponent. Linking the microscopic laws with the macroscopic ones, the SSD density ρ_S is

$$\rho_S = \left(\frac{\sigma_Y f(\varepsilon^p)}{M\alpha\mu b}\right)^2, \tag{17}$$

and from Eq. (14),

$$\sigma_{flow} = \sqrt{[\sigma_Y f(\varepsilon^p)]^2 + (M\alpha\mu b)^2\bar{r}\frac{\eta^p}{b}} = \sigma_Y\sqrt{f^2(\varepsilon^p) + l\eta^p} \tag{18}$$

where l is introduced as the material intrinsic length by Gao et al. [67], where

$$l = M^2\bar{r}\alpha^2\left(\frac{\mu}{\sigma_Y}\right)^2 b \approx 18\alpha^2\left(\frac{\mu}{\sigma_Y}\right)^2 b. \tag{19}$$

The calculation of the effective plastic strain gradient η^p in Eq. (13) is proposed by Gao et al. as

$$\eta^p = \sqrt{\frac{1}{4}\eta^p_{ijk}\eta^p_{ijk}}, \tag{20}$$

$$\eta^p_{ijk} = \varepsilon^p_{ik,j} + \varepsilon^p_{jk,i} - \varepsilon^p_{ij,k} \tag{21}$$

where ε^p_{ij} is the plastic strain tensor. The numerical calculation of η^p in an axisymmetric model could be referred to Swaddiwudhipong et al.'s work [45].

Huang et al. suggested a visco-plastic formula to relate the effective stress σ_e directly to the plastic strain rate $\dot{\varepsilon}^p$ to avoid the involvement of the higher-order effective stress rate $\dot{\sigma}_e$ by setting a large value of the exponent m, $m \geq 20$. Together with Eq. (18), the effective strain gradient is introduced by the flow stress as

$$\dot{\varepsilon}^p = \dot{\varepsilon}\left(\frac{\sigma_e}{\sigma_{\text{flow}}}\right)^m = \dot{\varepsilon}\left(\frac{\sigma_e}{\sigma_Y\sqrt{f^2(\varepsilon^p) + l\eta^p}}\right)^m \tag{22}$$

where $\dot{\varepsilon} = \sqrt{\frac{2}{3}\dot{\varepsilon}'_{ij}\dot{\varepsilon}'_{ij}}$ is the effective strain rate.

Thus, similar to the conventional plasticity theory, the strain rate is composed of the elastic part and the plastic part as

$$\dot{\varepsilon}_{ij} = \dot{\varepsilon}^e_{ij} + \dot{\varepsilon}^p_{ij} = \frac{1}{2\mu}\dot{\sigma}'_{ij} + \frac{\dot{\sigma}_{kk}}{9K}\delta_{ij} + \frac{3\dot{\varepsilon}^p}{2\sigma_e}\sigma'_{ij}, \tag{23}$$

and the elastic strain rate is

$$\dot{\varepsilon}^e_{ij} = \frac{1}{2\mu}\dot{\sigma}'_{ij} + \frac{\dot{\sigma}_{kk}}{9K}\delta_{ij} \tag{24}$$

where $\dot{\sigma}'_{ij}$ is the deviatoric stress rate, K the bulk modulus, and δ_{ij} the Kronecker delta. Hence, with $\dot{\varepsilon}_{kk} = \frac{\dot{\sigma}_{kk}}{3K}$, the deviatoric strain rate is

$$\dot{\varepsilon}'_{ij} = \dot{\varepsilon}_{ij} - \frac{1}{3}\dot{\varepsilon}_{kk}\delta_{ij} = \frac{1}{2\mu}\dot{\sigma}'_{ij} + \frac{3\dot{\varepsilon}^p}{2\sigma_e}\sigma'_{ij}, \tag{25}$$

Substituting Eq. (22) into Eq. (25), the deviatoric strain rate is related to the effective strain gradient by

$$\dot{\varepsilon}'_{ij} = \frac{1}{2\mu}\dot{\sigma}'_{ij} + \frac{3\dot{\varepsilon}}{2\sigma_e}\left(\frac{\sigma_e}{\sigma_Y\sqrt{f^2(\varepsilon^p) + l\eta^p}}\right)^m \sigma'_{ij} \tag{26}$$

which is commonly written as

$$\dot{\sigma}_{ij} = K\dot{\varepsilon}_{kk}\delta_{ij} + 2\mu\left[\dot{\varepsilon}'_{ij} - \frac{3\dot{\varepsilon}}{2\sigma_e}\left(\frac{\sigma_e}{\sigma_Y\sqrt{f^2(\varepsilon^p) + l\eta^p}}\right)^m \sigma'_{ij}\right]. \tag{27}$$

Equation (27) suggested by Huang et al. is the constitutive relation with the consideration of the plastic strain gradient by introducing a material intrinsic length. With this length-dimension parameter, the difference between size-scales of the material can be hence depicted. When $l \to 0$ or correspondingly the length scale of deformation is much larger than the material intrinsic length, the CMSG theory degenerates into the conventional theory.

References

1. Tabor, D.: The hardness and strength of metals. J. Inst. Met. **79**, 1 (1951)
2. Oliver, W.C., Pharr, G.M.: An improved technique for determining hardness and elastic modulus using load and displacement sensing indentation experiments. J. Mater. Res. **7**(6), 1564–1583 (1992). https://doi.org/10.1557/JMR.1992.1564
3. Lee, J.H., Kim, T., Lee, H.: A study on robust indentation techniques to evaluate elastic–plastic properties of metals. Int. J. Solids Struct. **47**(5), 647–664 (2010). https://doi.org/10.1016/j.ijsolstr.2009.11.003
4. Eswar Prasad, K., Chollacoop, N., Ramamurty, U.: Role of indenter angle on the plastic deformation underneath a sharp indenter and on representative strains: an experimental and numerical study. Acta Mater. **59**(11), 4343–4355 (2011). https://doi.org/10.1016/j.actamat.2011.03.058
5. Fischer-Cripps, A.C., Nicholson, D.W.: Nanoindentation. Mechanical engineering series. Appl. Mech. Rev. **57**(2), B12–B12 (2004). https://doi.org/10.1115/1.1704625
6. Broitman, E.: Indentation hardness measurements at macro-, micro-, and nanoscale: a critical overview. Tribol. Lett. **65**(1), 581 (2017). https://doi.org/10.1007/s11249-016-0805-5
7. Voyiadjis, G., Yaghoobi, M.: Review of nanoindentation size effect: experiments and atomistic simulation. Crystals **7**(10), 321 (2017). https://doi.org/10.3390/cryst7100321
8. Cheng, Y.-T., Cheng, C.-M.: Scaling approach to conical indentation in elastic–plastic solids with work hardening. J. Appl. Phys. **84**(3), 1284–1291 (1998). https://doi.org/10.1063/1.368196
9. Cheng, Y.-T., Cheng, C.-M.: Relationships between hardness, elastic modulus, and the work of indentation. Appl. Phys. Lett. **73**(5), 614–616 (1998). https://doi.org/10.1063/1.121873
10. Cheng, Y.-T., Cheng, C.-M.: Can stress–strain relationships be obtained from indentation curves using conical and pyramidal indenters? J. Mater. Res. **14**(9), 3493–3496 (1999). https://doi.org/10.1557/JMR.1999.0472
11. Cheng, Y.-T., Cheng, C.-M.: Scaling relationships in indentation of power-law creep solids using self-similar indenters. Philos. Mag. Lett. **81**(1), 9–16 (2001). https://doi.org/10.1080/09500830010008457
12. Cheng, Y.-T., Cheng, C.-M.: Scaling, dimensional analysis, and indentation measurements. Mater. Sci. Eng. R Rep. **44**(4–5), 91–149 (2004). https://doi.org/10.1016/j.mser.2004.05.001
13. Xiao, G., et al.: Determination of power hardening elastoplastic constitutive relation of metals through indentation tests with plural indenters. Mech. Mater. **138**, 103173 (2019). https://doi.org/10.1016/j.mechmat.2019.103173
14. Smerdova, O., Pecora, M., Gigliotti, M.: Cyclic indentation of polymers: Instantaneous elastic modulus from reloading, energy analysis, and cyclic creep. J. Mater. Res. **34**(21), 3688–3698 (2019). https://doi.org/10.1557/jmr.2019.289
15. Kang, G., Yan, W.: Scaling relationships in sharp conical indentation of shape memory alloys. Philos. Mag. **90**(5), 599–616 (2010). https://doi.org/10.1080/14786430903213346
16. Rodríguez, M., Molina-Aldareguía, J.M., González, C., LLorca, J.: Determination of the mechanical properties of amorphous materials through instrumented nanoindentation. Acta Mater. **60**(9), 3953–3964 (2012). https://doi.org/10.1016/j.actamat.2012.03.027
17. Bazzaz, E., Darvizeh, A., Alitavoli, M., Tooski, M.Y.: Implementation of the new minimum resultant error approach to extract elastic–plastic properties of titanium nitride thin film by nanoindentation, finite element analysis, and modified dimensional analysis. Proc. Inst. Mech. Eng. Part C J. Mech. Eng. Sci. **54**, 095440622091432 (2020). https://doi.org/10.1177/0954406220914326
18. Hamada, S., Kashiwa, S., Noguchi, H.: Measurement of local mechanical properties using multiple indentations by a special conical indenter and error analysis. J. Mater. Res. **31**(2), 259–273 (2016). https://doi.org/10.1557/jmr.2015.383
19. Pöhl, F.: Determination of unique plastic properties from sharp indentation. Int. J. Solids Struct. **171**, 174–180 (2019). https://doi.org/10.1016/j.ijsolstr.2019.04.008
20. Li, Y., Stevens, P., Sun, M., Zhang, C., Wang, W.: Improvement of predicting mechanical properties from spherical indentation test. Int. J. Mech. Sci. **117**, 182–196 (2016). https://doi.org/10.1016/j.ijmecsci.2016.08.019
21. Yu, Z., Wei, Y.: A study of indentation scaling relationships of elastic-perfectly plastic solids with an inclusion near the conical indenter tip. Sci. China Technol. Sci. **62**(5), 721–728 (2019). https://doi.org/10.1007/s11431-018-9424-4
22. Lu, L., Dao, M., Kumar, P., Ramamurty, U., Karniadakis, G.E., Suresh, S.: Extraction of mechanical properties of materials through deep learning from instrumented indentation. Proc. Natl. Acad. Sci. USA **117**(13), 7052–7062 (2020). https://doi.org/10.1073/pnas.1922210117
23. Zhang, M.-G., Cao, Y.-P., Li, G.-Y., Feng, X.-Q.: Spherical indentation method for determining the constitutive parameters of hyperelastic soft materials. Biomech. Model. Mechanobiol. **13**(1), 1–11 (2014). https://doi.org/10.1007/s10237-013-0481-4
24. Lee, H., Huen, W.Y., Vimonsatit, V., Mendis, P.: An investigation of nanomechanical properties of materials using nanoindentation and artificial neural network. Sci. Rep. **9**(1), 13189 (2019). https://doi.org/10.1038/s41598-019-49780-z
25. Lloyd, D.J.: Particle reinforced aluminium and magnesium matrix composites. Int. Mater. Rev. **39**(1), 1–23 (1994). https://doi.org/10.1179/imr.1994.39.1.1
26. Armstrong, R.W.: Size effects on material yield strength/deformation/fracturing properties. J. Mater. Res. **34**(13), 2161–2176 (2019). https://doi.org/10.1557/jmr.2018.406
27. Magonov, S.N., Elings, V., Whangbo, M.-H.: Phase imaging and stiffness in tapping-mode atomic force microscopy. Surf. Sci. **375**(2–3), L385–L391 (1997). https://doi.org/10.1016/S0039-6028(96)01591-9
28. Stegall, D.E., Mamun, M.A., Crawford, B., Elmustafa, A.: Indentation size effect in FCC metals: an examination of experimental techniques and the bilinear behavior. J. Mater. Res. **27**(12), 1543–1552 (2012). https://doi.org/10.1557/jmr.2012.91
29. Lucas, M., Gall, K., Riedo, E.: Tip size effects on atomic force microscopy nanoindentation of a gold single crystal. J. Appl. Phys. **104**(11), 113515 (2008). https://doi.org/10.1063/1.3039511
30. Ni, H., Li, X.: Young's modulus of ZnO nanobelts measured using atomic force microscopy and nanoindentation techniques. Nanotechnology **17**(14), 3591–3597 (2006). https://doi.org/10.1088/0957-4484/17/14/039

31. Jee, A.-Y., Lee, M.: Comparative analysis on the nanoindentation of polymers using atomic force microscopy. Polym. Test. **29**(1), 95–99 (2010). https://doi.org/10.1016/j.polymertesting.2009.09.009
32. Fischer-Cripps, A.C.: Critical review of analysis and interpretation of nanoindentation test data. Surf. Coat. Technol. **200**(14–15), 4153–4165 (2006). https://doi.org/10.1016/j.surfcoat.2005.03.018
33. Lin, Z., Yu, Z., Wei, Y.: Measurement of nanoindentation properties of polymers considering adhesion effects between AFM sharp indenter and material. J. Adhes. Sci. Technol. **38**(3), 1–18 (2020). https://doi.org/10.1080/01694243.2020.1714117
34. Long, X., Jia, Q.P., Li, Z., Wen, S.X.: Reverse analysis of constitutive properties of sintered silver particles from nanoindentations. Int. J. Solids Struct. **191–192**, 351–362 (2020). https://doi.org/10.1016/j.ijsolstr.2020.01.014
35. Swadener, J.G., George, E.P., Pharr, G.M.: The correlation of the indentation size effect measured with indenters of various shapes. J. Mech. Phys. Solids **50**(4), 681–694 (2002). https://doi.org/10.1016/S0022-5096(01)00103-X
36. Liu, M., Lu, C., Tieu, K.A., Peng, C.-T., Kong, C.: A combined experimental-numerical approach for determining mechanical properties of aluminum subjects to nanoindentation. Sci. Rep. **5**, 15072 (2015). https://doi.org/10.1038/srep15072
37. Jiapeng, S., Cheng, L., Han, J., Ma, A., Fang, L.: Nanoindentation induced deformation and pop-in events in a silicon crystal: molecular dynamics simulation and experiment. Sci. Rep. **7**(1), 10282 (2017). https://doi.org/10.1038/s41598-017-11130-2
38. Zhou, X., et al.: High-pressure strengthening in ultrafine-grained metals. Nature **579**(7797), 67–72 (2020). https://doi.org/10.1038/s41586-020-2036-z
39. Yang, R., et al.: The significance and challenges on determining the size-effect of indentation hardness at nano-scale. Sci. Sin. Phys. Mech. Astron. **48**(9), 94603 (2018). https://doi.org/10.1360/SSPMA2018-00206
40. Gouldstone, A., Chollacoop, N., Dao, M., Ll, J., Minor, A., Shen, Y.: Indentation across size scales and disciplines: Recent developments in experimentation and modeling. Acta Mater. **55**(12), 4015–4039 (2007). https://doi.org/10.1016/j.actamat.2006.08.044
41. Huang, Y., Qu, S., Hwang, K.C., Li, M., Gao, H.: A conventional theory of mechanism-based strain gradient plasticity. Int. J. Plast. **20**(4–5), 753–782 (2004). https://doi.org/10.1016/j.ijplas.2003.08.002
42. Nix, W.D., Gao, H.: Indentation size effects in crystalline materials: a law for strain gradient plasticity. J. Mech. Phys. Solids **46**(3), 411–425 (1998). https://doi.org/10.1016/S0022-5096(97)00086-0
43. Martínez-Pañeda, E., Betegón, C.: Modeling damage and fracture within strain-gradient plasticity. Int. J. Solids Struct. **59**, 208–215 (2015). https://doi.org/10.1016/j.ijsolstr.2015.02.010
44. Martínez-Pañeda, E., Niordson, C.F.: On fracture in finite strain gradient plasticity. Int. J. Plast. **80**, 154–167 (2016). https://doi.org/10.1016/j.ijplas.2015.09.009
45. Swaddiwudhipong, S., Tho, K.K., Hua, J., Liu, Z.S.: Mechanism-based strain gradient plasticity in C0 axisymmetric element. Int. J. Solids Struct. **43**(5), 1117–1130 (2006). https://doi.org/10.1016/j.ijsolstr.2005.05.026
46. Smith, M.:*ABAQUS/Standard User's Manual, Version 6.14*. Pawtucket, Rhode Island (2014).
47. Brand, L.: The Pi theorem of dimensional analysis. Arch. Ration. Mech. Anal. **1**(1), 35–45 (1957)
48. Bhattacharya, A.K., Nix, W.D.: Finite element simulation of indentation experiments. Int. J. Solids Struct. **24**(9), 881–891 (1988). https://doi.org/10.1016/0020-7683(88)90039-X
49. Cheng, Y.-T., Li, Z., Cheng, C.-M.: Scaling relationships for indentation measurements. Philos. Mag. A **82**(10), 1821–1829 (2002). https://doi.org/10.1080/01418610208235693
50. Laursen, T.A., Simo, J.C.: A study of the mechanics of microindentation using finite elements. J. Mater. Res. **7**(3), 618–626 (1992). https://doi.org/10.1557/JMR.1992.0618
51. Zhang, F., Hwang, K.C., Huang, Y.G., Qin, J.: Friction effect on indentation. Gongcheng Lixue/Eng. Mech. **23**(Suppl), 1–6 (2006)
52. Trelewicz, J.R., Schuh, C.A.: The Hall–Petch breakdown in nanocrystalline metals: a crossover to glass-like deformation. Acta Mater. **55**(17), 5948–5958 (2007). https://doi.org/10.1016/j.actamat.2007.07.020
53. Dang, S., Zhu, Q.-L., Xu, Q.: Nanomaterials derived from metal–organic frameworks. Nat. Rev. Mater. **3**(1), 10667 (2018). https://doi.org/10.1038/natrevmats.2017.75
54. Barenblat, G.: Scaling, Self-Similarity and Intermediate Asymptotics. CUP, Cambridge (1996)
55. Mata, M., Alcalá, J.: The role of friction on sharp indentation. J. Mech. Phys. Solids **52**(1), 145–165 (2004). https://doi.org/10.1016/S0022-5096(03)00075-9
56. Wei, Y., Shu, S., Du, Y., Zhu, C.: Size, geometry and nonuniformity effects of surface-nanocrystalline aluminum in nanoindentation test. Int. J. Plast **21**(11), 2089–2106 (2005). https://doi.org/10.1016/j.ijplas.2005.04.002
57. Swadener, J.G., George, E.P., Pharr, G.M.: The correlation of the indentation size effect measured with indenters of various shapes. J. Mech. Phys. Solids **50**, 681–694 (2002)
58. Shell De Guzman, M., Neubauer, G., Flinn, P., Nix, W.D.: The role of indentation depth on the measured hardness of materials. MRS Proc. **308**, 12 (1993). https://doi.org/10.1557/PROC-308-613
59. Bull, S.J.: On the origins and mechanisms of the indentation size effect. MEKU **94**(7), 787–792 (2003). https://doi.org/10.3139/146.030787
60. Kim, J.-Y., Kang, S.-K., Lee, J.-J., Jang, J.-I., Lee, Y.-H., Kwon, D.: Influence of surface-roughness on indentation size effect. Acta Mater. **55**(10), 3555–3562 (2007). https://doi.org/10.1016/j.actamat.2007.02.006
61. McElhaney, K.W., Vlassak, J.J., Nix, W.D.: Determination of indenter tip geometry and indentation contact area for depth-sensing indentation experiments. J. Mater. Res. **13**(5), 1300–1306 (1998). https://doi.org/10.1557/JMR.1998.0185
62. Ma, Q., Clarke, D.R.: Size dependent hardness of silver single crystals. J. Mater. Res. **10**(4), 853–863 (1995). https://doi.org/10.1557/JMR.1995.0853
63. Wei, Y., Wang, X., Xiaolei, Wu., Bai, Y.: Theories and experiments of size-effect in indentation. Sci. China Ser. A Math. **30**(11), 1025–1032 (2000). https://doi.org/10.1360/za2000-30-11-1025
64. Fleck, N.A., Hutchinson, J.W.: A phenomenological theory for strain gradient effects in plasticity. J. Mech. Phys. Solids **41**, 1825–1857 (1993)
65. Shu, J.Y., Barlow, C.Y.: Strain gradient effects on microscopic strain field in a metal matrix composite. Int. J. Plast. **16**(5), 563–591 (2000). https://doi.org/10.1016/S0749-6419(99)00088-1

66. Wei, Y., Hutchinson, J.W.: Steady-state crack growth and work of fracture for solids characterized by strain gradient plasticity. J. Mech. Phys. Solids **45**(8), 1253–1273 (1997). https://doi.org/10.1016/S0022-5096(97)00018-5
67. Gao, H., Huang, Y., Nix, W.D., Hutchinson, J.W.: Mechanism-based strain gradient plasticity I. Theory. J. Mech. Phys. Solids **47**(6), 1239–1263 (1999). https://doi.org/10.1016/S0022-5096(98)00103-3
68. Huang, Y., Gao, H., Nix, W.D., Hutchinson, J.W.: Mechanism-based strain gradient plasticity II. Analysis. J. Mech. Phys. Solids **48**, 99–128 (2000)
69. Taylor, G.I.: The mechanism of plastic deformation of crystals part I—theoretical. Proc. R. Soc. Lond. Ser. A **145**(885), 362–387 (1934)
70. Taylor, G.I.: Plastic strain in metals. J. Inst. Metals **62**, 307–324 (1938)
71. Qu, S., Huang, Y., Jiang, H., Liu, C., Wu, P.D., Hwang, K.C.: Fracture analysis in the conventional theory of mechanism-based strain gradient (CMSG) plasticity. Int. J. Fract. **129**, 199–220 (2004)
72. Song, H., van der Giessen, E., Liu, X.: Strain gradient plasticity analysis of elasto-plastic contact between rough surfaces. J. Mech. Phys. Solids **96**, 18–28 (2016). https://doi.org/10.1016/j.jmps.2016.07.00